ENVIRONMENTAL RESEARCH
ECOLOGY

PURPOSE-LED PUBLISHING™

Part of the ENVIRONMENTAL RESEARCH SERIES

PAPER • OPEN ACCESS

Detecting unvegetated permafrost-thaw features in Arctic tundra using imaging spectroscopy

To cite this article: F Tenorio *et al* 2026 *Environ. Res.: Ecology* **5** 015007

ENVIRONMENTAL RESEARCH
ECOLOGY

OPEN ACCESS

RECEIVED
7 February 2025

REVISED
9 February 2026

ACCEPTED FOR PUBLICATION
20 February 2026

PUBLISHED
5 March 2026

PAPER

Detecting unvegetated permafrost-thaw features in Arctic tundra using imaging spectroscopy

F Tenorio[1,2,3,*], D Sousa[1], J Hashemi[4], S J Davidson[5], W C Oechel[1], C E Tweedie[6], B D Thomas[7], S Rauschenbach[8] and D Zona[1]

[1] Department of Biology and Department of Geography, San Diego State University, San Diego, CA 92182, United States of America
[2] NOAA EPP Center for Earth System Sciences and Remote Sensing Technologies II, New York, NY, United States of America
[3] Department of Plant Sciences, University of California at Davis, Davis, CA 95616, United States of America
[4] Alfred Wegener Institute Helmholtz Centre for Polar and Marine Research, Potsdam 14473, Germany
[5] Département des sciences biologiques, Université du Québec à Montréal, Montréal, QC, Canada
[6] Department of Biological Sciences, University of Texas at El Paso, El Paso, TX 79902, United States of America
[7] NOAA Barrow Atmospheric Baseline Observatory, P.O. Box 888, Utqiaġvik, AK 99723-0888, United States of America
[8] University of California, Davis, Atmospheric Science Graduate Group, Davis, CA 95616, United States of America
[*] Author to whom any correspondence should be addressed.

E-mail: ftenorio2833@sdsu.edu

Keywords: imaging spectroscopy, Arctic, unvegetated thermokarst polygons, spectral unmixing, hyperspectral, permafrost degradation, biogeochemical cycling

Supplementary material for this article is available online

Abstract

Freeze-thaw cycles, hydrology, soil mixing, and permafrost degradation shape landscape patterns in permafrost regions, forming unvegetated or sparsely vegetated landforms with varied topography. These features, which we refer to as unvegetated thermokarst polygons, result from permafrost thaw and may play a critical role in Arctic greenhouse gas (GHG) dynamics by unlocking vast amounts of carbon stored in permafrost regions. However, their spatial extent remains uncertain due to their variable size (∼0.5–15 m) and the challenges of detecting them in heterogeneous landscapes such as polygonal tundra. This study assesses the extent of unvegetated thermokarst polygons near Utqiaġvik, Alaska, using imaging spectroscopy and lidar data with a 1 m spatial resolution from the National Ecological Observing Network airborne observation platform on the joint-basis of a linear spectral mixture analysis and lidar-based relief. Based on a confusion matrix evaluating threshold models of our analysis against field-based results, the model that performed with the greatest $F1$ score (0.63), with balanced precision (0.71) and recall (0.57), estimated a 9.55% cover of unvegetated thermokarst polygons, or 380 000 m^2 total area of unvegetated thermokarst polygons within the study extent. Ground truth data from 52 sites revealed that the spectral mixture model correctly mapped ∼81% of unvegetated thermokarst polygons. Our results highlight the challenges and potential of detecting unvegetated thermokarst polygons in complex Arctic landscapes with high-resolution remote sensing. Although these features currently cover a small area in the study site, their relevance may grow with increased landscape changes and GHG dynamics under warm conditions. Moreover, their extent could be greater in areas with more active permafrost degradation, emphasizing the need for detection methods to monitor these critical landforms.

1. Introduction

Arctic regions have warmed nearly four times the global mean average temperature (Rantanen *et al* 2022). These regions are vital ecosystems, as they regulate climate via the carbon budget and energy balance (Oechel *et al* 1993, Kaplan *et al* 2003). Ecosystems within the Arctic consist of permafrost, a subsurface earth material such as soil and rock that remains at or below 0 °C for two or more consecutive years (Muller 1943, National Research Council 2014, Fiencke *et al* 2022). Permafrost soils comprise one of the largest terrestrial reservoirs of carbon (C) and nitrogen (N), holding over half of all the estimated soil organic matter (Hugelius *et al* 2014, Abbott and Jones 2015, Chowdhury *et al* 2015). As permafrost thaws, soil organic carbon becomes vulnerable to decomposition, resulting in the emission of greenhouse gases (GHGs), carbon dioxide (CO_2), methane (CH_4), and nitrous oxide (N_2O) by microbial activity (Harden *et al* 2012, Yang *et al* 2018, Voigt *et al* 2020).

Permafrost thaw also has an impact on the topography of Arctic ecosystems, forming highly diverse landscapes (Lachenbruch 1962, Hinkel *et al* 2003, Jones *et al* 2011, Liljedahl *et al* 2016). One of the most prominent consequences of thaw is land surface subsidence, known as thermokarst, which generates distinctive landforms such as thermokarst lakes, polygons, bogs, and fens (Péwé 1954, Kokelj and Jorgenson 2013, Olefeldt *et al* 2016). Among these, thermokarst polygons are particularly important due to the high carbon content in thermokarst regions and significant N_2O emissions in unvegetated areas of the polygons with active erosion layers (e.g. bare, collapsed, and cracked soil), which arise from limited plant competition for inorganic N (Hashemi *et al* 2024). These unvegetated thermokarst polygons also emit significant CO_2 emissions, likely caused by the lack of CO_2 uptake through photosynthesis, with ecosystem respiration as the end result (Hashemi *et al* 2024). Given the role that permafrost landscapes serve as a significant carbon and nitrogen reservoir and the heightened vulnerability to climate warming at high northern latitudes, quantifying landscape features such as thermokarst polygons is likely crucial for understanding carbon dynamics and their implications for global climate change.

Thermokarst-affected landscapes cover approximately $\sim$20% of the Arctic and store approximately 50% of the region's organic carbon, making them critical to Arctic carbon cycling (Jones *et al* 2011, Olefeldt *et al* 2016). Thermokarst processes are driven by the melting of excess ice in the soil, which can occur gradually through the deepening of the active layer or abruptly during rapid thaw events (Muller 1947, Péwé 1954, Van Everdingen 1998, Olefeldt *et al* 2016). These processes influence macro-scale and micro-scale topography, creating a mosaic of landforms that vary in hydrology, vegetation, and carbon storage potential (Kokelj and Jorgenson 2013, Olefeldt *et al* 2016). Cryoturbation, the mixing and disturbance of soil horizons due to frost action (Bryan 1946, Bockheim and Tarnocai 1998), further shapes these landscapes, contributing to the formation of features such as frost boils, bare palsa surfaces, peat circles, and unvegetated thermokarst areas (Peterson and Krantz 2008, Repo *et al* 2009, Marushchak *et al* 2011, Hashemi *et al* 2024). A distinctive feature of the landscape is polygonal tundra, which forms with the development of ice wedges in some continuous permafrost regions as part of the freeze-thaw cycle (Liljedahl *et al* 2016). Ice wedges form over a prolonged period (timescales from centuries to millennia), giving rise to surface relief as they grow and develop (Leffingwell 1915, Liljedahl *et al* 2016). This development creates unique polygonal patterns (Lachenbruch 1962, Liljedahl *et al* 2016).

Ice-wedges contribute to the formation of polygonal terrain in which the polygons start as low-centered polygons (LCPs), which are approximately 5–30 m in diameter, and eventually become high-centered polygons (HCPs) that can develop into well-drained mounds that protrude above the water table and become surrounded by troughs (Britton 1957, Péwé 1969, Billings and Peterson 1980, Liljedahl *et al* 2016). The formation and life cycle of polygons is a highly debated topic (Shur *et al* 2025) in which the development of LCPs is considered a critical landform for understanding the evolution of polygonal landscapes (Shur *et al* 2025). The implication of polygons evolving from LCPs to HCPs can impact carbon storage over time by potentially releasing carbon that has remained locked in thermokarst regions (Olefeldt *et al* 2016). In recent years, increasing ice-wedge degradation has led to the expansion of trough networks in some Arctic landscapes, altering hydraulic connectivity and carbon dynamics (Liljedahl *et al* 2016, Kanevskiy *et al* 2017). In particular, unvegetated thermokarst polygons typically found on HCPs (Hashemi *et al* 2024), which are the result of freeze-thaw cycles, ice wedge dynamics, and hydrological interactions (Hashemi *et al* 2024), are less well understood. These features tend to protrude above the water table and are sparsely vegetated with a large percentage cover of dark, organic-rich, and peat-like soil due to degradation on HCPs caused by the destabilization of the coupled interactions mentioned above (Hashemi *et al* 2024). Chamber studies focusing on unvegetated thermokarst polygons have demonstrated their potential for emitting significant CO_2 and N_2O emissions from these features (Hashemi *et al* 2024).

Remote sensing has become a useful tool for monitoring thermokarst processes, particularly in remote Arctic regions, where field access is challenging. Advances in both the platform and sensing technologies associated with aerial photography, airborne imaging, and satellite imagery have improved the observation of permafrost dynamics and thermokarst features over decadal timescales, providing critical insights into dramatically changing Arctic landscapes (Jorgenson *et al* 2006, Kokelj and Jorgenson 2013, Olefeldt *et al* 2016, Nelson *et al* 2022). For instance, remote sensing has been used to map drained lake basins, which cover at least 50% of the Arctic Coastal Plain of Alaska, and to classify these basins based on drainage timing, a key factor affecting a full range of environmental characteristics (Hinkel *et al* 2003). Similarly, the expansion of thermokarst lakes, vegetation landscape change, and the degradation of ice wedges have been documented using time-series satellite and airborne imagery (Jones *et al* 2011, Lin *et al* 2012, Liljedahl *et al* 2016, Kanevskiy *et al* 2017, Lara *et al* 2019, 2021). Other studies have also highlighted the role of infrastructure in destabilizing permafrost, as seen in the Prudhoe Bay Oilfield region, where thermokarst features and ice-wedge degradation have expanded in built-up areas (Raynolds *et al* 2014, Kanevskiy *et al* 2022).

While much of the remote sensing research on thermokarst processes has focused on macrotopographic features—drained lake basins, hillslope thermokarst, and thermo-erosional gullies (Hinkel *et al* 2003, Jones *et al* 2011, Kokelj and Jorgenson 2013, Liu *et al* 2014, Olefeldt *et al* 2016)—fewer studies have investigated microtopographic features such as HCPs, LCPs, troughs, pits, and thermokarst polygons (Jorgenson *et al* 2006, Lara *et al* 2015, Liljedahl *et al* 2016, Kanevskiy *et al* 2017, Abolt and Young 2020). Previous work on employing remote sensing techniques to map the microtopography of polygonal terrain includes, but is not limited to, characterization of multiscale zonation in polygons via airborne-derived DEM (Wainwright *et al* 2015). Researchers have used UAV and photogrammetric surveys to delineate and characterize ice-wedge polygonal networks. This method allows for quantitative verification of extracted features across different spatial resolutions using high-resolution imagery (Lousada *et al* 2018). Other approaches include automation with the introduction of machine learning applications, such as using deep learning convolutional neural networks, complemented with high-resolution aerial imagery to characterize ice-wedge polygons at Pan-Arctic scales (Zhang *et al* 2018). The introduction of high spatial commercial satellite imagery has also been used in automation techniques, including the development of automatic workflows to extract ice-wedge polygon troughs on sedge tundra and tussock tundra (Witharana *et al* 2021). Convolutional neural networks have also been used in the mapping of common polygon networks found in ice-wedge landscapes, consisting of target classes such as open water, polygonal wetland, and upland terrain, by fusing together synthetic aperture radar data (SAR) with ArcticDEM topographic data (Merchant *et al* 2024).

These studies present both the successes and challenges of quantifying and detecting microtopography in polygonal Arctic ecosystems. Challenges for mapping polygons include the geoecological complexity of permafrost landscapes, which includes highly heterogeneous vegetation and landforms (Kokelj and Jorgenson 2013, Nelson *et al* 2022). Furthermore, collecting satellite remote sensing data in high-latitude ecosystems, such as the Arctic Coastal Plain of Alaska, is temporally limited by these regions' long, severe, and dark winters (Stow *et al* 2004). Optical remote sensing data can only feasibly be collected during short, often cloudy summers, and most available datasets lack the meter-to-submeter spatial resolution required to map microtopography (Kokelj and Jorgenson 2013, Nelson *et al* 2022). As a result, the extent and location of smaller-scale features such as unvegetated thermokarst polygons investigated in this study remain poorly quantified. Current estimates of thermokarst-affected landforms (20% of the northern permafrost region) do not explicitly include unvegetated thermokarst polygons (Olefeldt *et al* 2016).

This study quantifies the extent of unvegetated thermokarst polygons within the Barrow Environmental Observatory (BEO) near the city of Utqiaġvik (formerly Barrow), Alaska. Specifically, analyses sought to detect HCPs with active erosion layers that might result in collapsing unvegetated thermokarst polygons given their significant emissions in CO_2 and N_2O (Hashemi *et al* 2024). To approach this problem, we use a novel technique of fusing together 1 m-resolution hyperspectral imaging and lidar acquired by the National Ecological Observatory Network (NEON) airborne observation platform (AOP). We delineate the location and percent cover of unvegetated thermokarst polygons using endmember (EM) fractions from a spectral mixture model fraction and lidar-based relief. Additionally, we incorporate vegetation community data to explore landscape patterns associated with unvegetated thermokarst polygons and examine their potential development to drained lake basins within the study area.

2. Materials and methods

2.1. Study site

The study site (figure 1) is in the BEO (71.28°N, 156.61°W), located approximately 6 km southeast of Utqiaġvik, consisting of well-developed HCPs and LCPs tundra (Zona *et al* 2009, Davidson *et al* 2016a). The landscapes found here stand out for their characteristic patterns, consisting of drained lake basins and highly heterogeneous vegetation reflecting variation in microtopography (Zona *et al* 2009, Villarreal *et al* 2012, Arndt *et al* 2019). This area has been set aside for research and is protected by the Ukpeaġvik

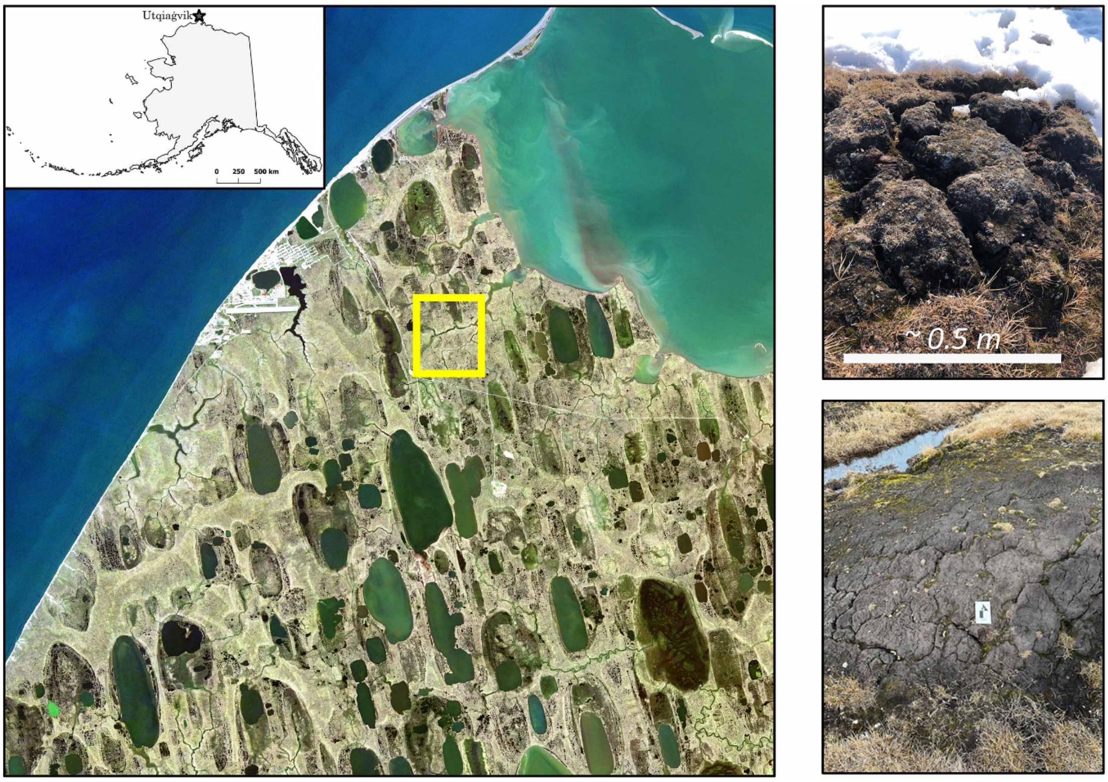

Figure 1. An overview of the study area showing the location of Utqiaġvik in Alaska, represented by the gray star (source: www.census.gov/) via QGIS. True color RGB satellite image collected by RapidEye (© 2018 Planet Labs); the study area extent is highlighted by the yellow box (left). Unvegetated thermokarst polygons in the BEO (right), landforms vary in size and vegetation cover.

Iñupiat Corporation. The region's climate is characterized by short summers and long winters (NOAA National Centers for Environmental Information 2023).

The vegetation within the BEO is predominantly wet-graminoid-moss communities (Raynolds *et al* 2005, Lara *et al* 2015, Davidson *et al* 2016a). Due to the high heterogeneity within our study site, flora varies depending on several factors, such as soil moisture (Brown *et al* 1980, Villarreal *et al* 2012). For instance, HCPs often consist of moss lichens, with species such as *Polytrichum* and *Carex* graminoid tundra (Villarreal *et al* 2012, Davidson *et al* 2016a). *Carex aquatilis* and *Eriophorum russeolum* dominate the rims of HCPs (Villarreal *et al* 2012, Davidson *et al* 2016a). *Sphagnum* mosses, *Carex, Luzula, Poa, Dupontia,* and *Eriophorum* are common in LCPs and polygon troughs (Villarreal *et al* 2012, Davidson *et al* 2016a). Soils are classified as gelisols, with reworked glaciomarine sediments of the Pleistocene age as the parent material (Black 1964, Brown *et al* 1980, Bockheim *et al* 1999).

2.2. Remote sensing data products

Imaging spectroscopy was used to map small (submeter-to-meter scale) unvegetated thermokarst polygons. A conceptual approach was developed to identify these features based on two criteria: (1) local topographic relief and (2) lack of photosynthetic vegetation. It was assumed that areas meeting both criteria might be probable sites of unvegetated thermokarst polygons. During validation of these features in the field, features were classified as unvegetated thermokarst polygons if the feature consisted of $\geqslant$8 inches in diameter of dark, barren soil with little to no vegetation, and were located in HCPs or soil mounds, along with the presence of collapsing signs such as cracks and eroding soil.

Airborne lidar and imaging spectroscopy data collected by the NEON AOP over the Utqiaġvik NEON (BARR) site were used for this study. NEON AOP data are collected at flight altitudes of approximately 1000 m and flight speeds of roughly 50 ms^{-1}. Imaging spectroscopy data were collected with an approximately 100 ms integration time and one milliradian instantaneous field of view, resulting in approximately 1 m ground sampling distance. More details and flight reports can be found at www.neonscience.org/data-collection/daily-flight-reports. This analysis used flight lines collected on July 11th, 2018, with a 40.71°solar elevation and partly cloudy atmospheric conditions. Partly cloudy atmospheric conditions can lead to difficulty in interpreting reflectance values if not accounted for due to clouds' high reflectivity and wide variability in absorptivity across wavelengths. The NEON AOP data used in our study are an atmospherically corrected product, including many QA and ancillary rasters. NEON AOP accounts for partly cloudy conditions using the atmospheric and topographic correction algorithm.

Both imaging spectroscopy and lidar data are distributed on 1 m pixel grids. Four tiles of orthorectified surface reflectance (DP3.30006.001) and lidar (DP3.30024.001) digital surface model (DSM) were compiled into mosaics for our study, covering the central area of the BEO (NW: 156.62 W, 71.28 N; NE: 156.57 W, 71.28 N; SW: 156.62 W, 71.26 N; SE: 156.57 W, 71.26 N). The orthorectified surface reflectance product has a 5 nm spectral resolution in over 420 bands from 380 to 2500 nm, all of which were included in our study. The lidar data are distributed and acquired at a minimum density of 4 lidar shots per square meter in non-overlap areas. NEON AOP lidar returns are full waveforms, from which up to 5 points per shot may be discretized. Imaging spectroscopy and lidar data were used as-is without additional correction for bidirectional reflectance distribution function effects.

In addition, our study incorporated barrow area information database (BAID) wetlands map data products (Tweedie *et al* 2016) to determine the main vegetation communities within our study extent and Hinkel *et al*'s (2003) age of drained lake basins map data to better understand the ecological conditions of the unvegetated thermokarst polygons located during the field validation. Both of these data products were used as is, and maps were made using ArcGIS Pro 3.0.3 Copyright ©2022 Esri Inc. By overlaying the coordinates from our field validation surveys to the BAID wetlands map and Hinkel *et al*'s (2003) age of drained lake basins map.

2.3. SMA mixture analysis

Given the polygonized tundra's high fine-scale spatial heterogeneity, mixed pixels dominate Arctic tundra landscapes even at 1 m spatial resolution (Nelson *et al* 2022). Hence, we mapped sparsely vegetated thermokarst polygons with unvegetated surfaces for this study using linear SMA (Adams *et al* 1986, Gillespie 1990, Smith *et al* 1990). SMA treats the reflectance measurement at each pixel as a linear combination of spectral EM materials plus misfit. For more background on using SMA for landscape analysis, see Adams and Gillespie (2006).

Local EMs were manually selected from the spectral feature space of our reflectance mosaic, following Boardman (1995). The Boardman (1995) technique is used to help identify and map materials based on their spectral signatures. In this method, dimensionality analysis and noise whitening process, using the minimum noise fraction transform process, is applied to the imagery (Boardman 1995). We applied this approach to select the local EMs from our reflecting mosaic using ENVI® classic V.5.6.3. ENVI® is a registered trademark of NV5 Global, Inc. Consistent with previous compilations of airborne (Sousa & Small 2019, Sousa *et al* 2022) and satellite imaging spectroscopy (Sousa and Small 2023), the spectral feature space for this analysis was bounded by soil and non-photosynthetic vegetation substrates such as senescent plant material, dwarf shrub branches, and litter (S), illuminated photosynthetic vegetation (V), and dark targets, such as shadow and water (D). The reflectance mosaic was then unmixed using S, V, and D EMs as the basis of a linear mixture model with a unit sum constraint = 1 (figure 2) (Settle and Drake 1993).

The unmixing procedure was followed by layer stacking the unmixed reflectance mosaic with the overlapping lidar mosaic, combining both the lidar band and the raster bands from the unmixed image into a single file for classification of unvegetated thermokarst polygons. Potential sites hosting unvegetated thermokarst polygons were manually selected on the basis of elevation (lidar) and the unmixed mapped S pixels via 2D scatter plots by selecting the lidar band and the S band from the layer stacked unmixed image. Regions in the point cloud space of the 2D scatter plot that contained the highest frequency of S EM and lidar band throughout the study scene were selected and exported as regions of interests (ROIs). These ROIs were then classified as unvegetated thermokarst polygons within the study scene. All data imaging analyses were performed using ENVI® classic V.5.6.3. ENVI® is a registered trademark of NV5 Global, Inc.

2.4. Field surveys

Field validation data were collected during the summer field seasons of 2022, 2023, and 2025. Surveys began in late June, coinciding with the latter stages of snowmelt when the unvegetated thermokarst polygons were most easily identifiable, and continued through mid-August.

Based on the unmixing analysis (figure 2), the study area was divided into six clusters, which were stratified by the SMA results from the unmixed layer stacked image detecting probable unvegetated thermokarst polygons. Four of the six clusters (C1, C2, C4, and C5, see figure 3) were accessible by foot and selected for field-based validation during the 2022 and 2023 field surveys; an additional two clusters near C1 were included in the 2025 field survey (C1a and C1b, figure 2) to collect additional field validation

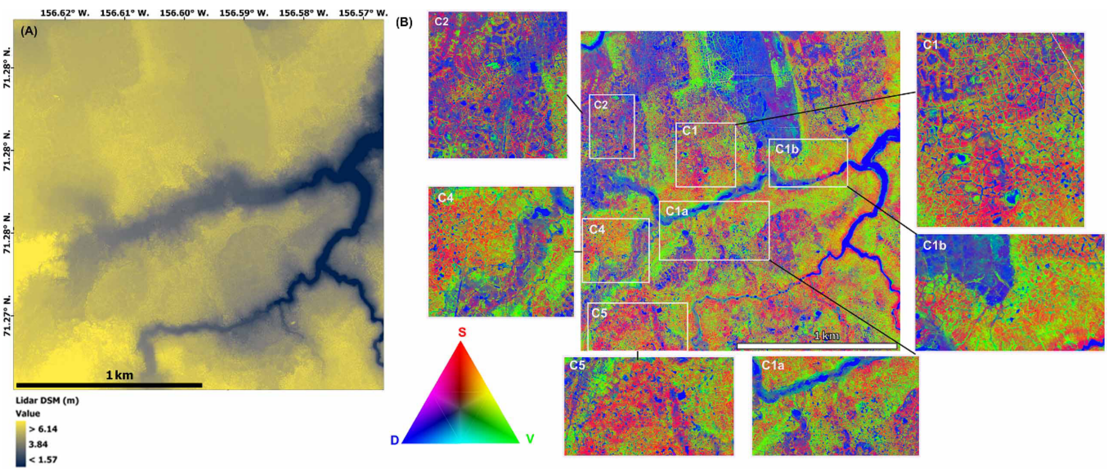

Figure 2. (A) DSM of the extent of the study site using NEON AOP Lidar (product: DP3.30024.001). (B) Spectral mixture analysis of the study area was created using NEON AOP hyperspectral reflectance (product: DP3.30006.001). The colors represent endmembers used in our analysis: red pixels are associated with soil substrates or non-photosynthetically active materials (S), blue pixels are associated with dark targets such as shadows or water (D), and green pixels are associated with photosynthetically active materials such as vegetation (V). Zoomed-in areas are representative of the clusters C1, C2, C4, and C5 visited for field validation during the surveys in 2022 and 2023. Clusters C1a and C1b are the additional clusters validated during the 2025 field survey.

data. The remaining clusters were excluded due to logistical constraints such as rugged terrain and limited access by foot.

During the surveys, fifty-two sites were visited across the clusters. These sites were chosen based on the classification from the unmixing analysis detecting unvegetated thermokarst polygons mentioned in section 2.3 on an aggregate pixel basis (e.g. the black pixels shown in figure 3, panel B).

An image and coordinates were recorded at each site using Global Positioning System (GPS) to retrieve position via a navigation app (Gaia GPS) as a form of validation of the black pixels mapping unvegetated thermokarst polygons. Differential GPS (dGPS) static surveys were collected at forty-six of the fifty-two sites across two field campaigns: the summer of 2022 and the summer of 2025. A Trimble 5700/R7 Campaign Kit (Trimble Inc., Westminster, CO, USA) was used during the 2022 field survey for a total of fifteen sites. A STONEX S900A GNSS Receiver was used during the 2025 field survey for a total of thirty-one sites. The dGPS data from 2022 were collected at a logging interval of 1.0 s for a minimum of fifteen minutes and up to forty-four minutes. GPS data from the BARO base station, downloaded during the occupational times of dGPS surveys, served as the known reference point to solve the locations sampled during field validation surveys. The dGPS data from 2025 were collected at a logging interval of 1.0 s and were used as is without processing to a base station, with an accuracy of $\sim$1 m roughly.

The spectral signatures from the NEON AOP dataset, used in our unmixing workflow, were tied to site locations and are included in the supplementary material. Spectral signatures in the field were obtained from unvegetated thermokarst polygons and misclassified sites during 2023 for a total of 19 sites using a handheld Spectra Vista Corporation (SVC) Spectroradiometer HR-512i (SVC, Poughkeepsie, NY, USA). The instrument measures reflectance at a wavelength range of 350–1035 nm at a spectral resolution of $\leqslant$3.2 nm full width at half maximum @ 700 nm and a total of 512 bands.

2.5. Decision rules

To estimate the surface composition in the scene, we visually inspected S, V, and D bands from the unmixed classified image, masking out infrastructure-related pixels under three thresholds: conservative (90%), intermediate (70%), and liberal (50%). The rationale for each threshold was chosen based on field checks conducted during the field surveys of the study area. Selecting thresholds from a conservative (90%) to liberal (50%) estimate enabled investigation of a representative spectrum of possible outcomes that could be compared to the ground truth data. The liberal thresholds for each band were chosen based on visual inspections to determine peak pixel frequency for each EM band via histogram distributions. The same approach was taken for the conservative and intermediate thresholds, in which the frequency of materials decreased as our thresholds became conservative. A full table showing all the possible threshold combinations along with surface composition for each EM and histograms is provided in the supplementary materials.

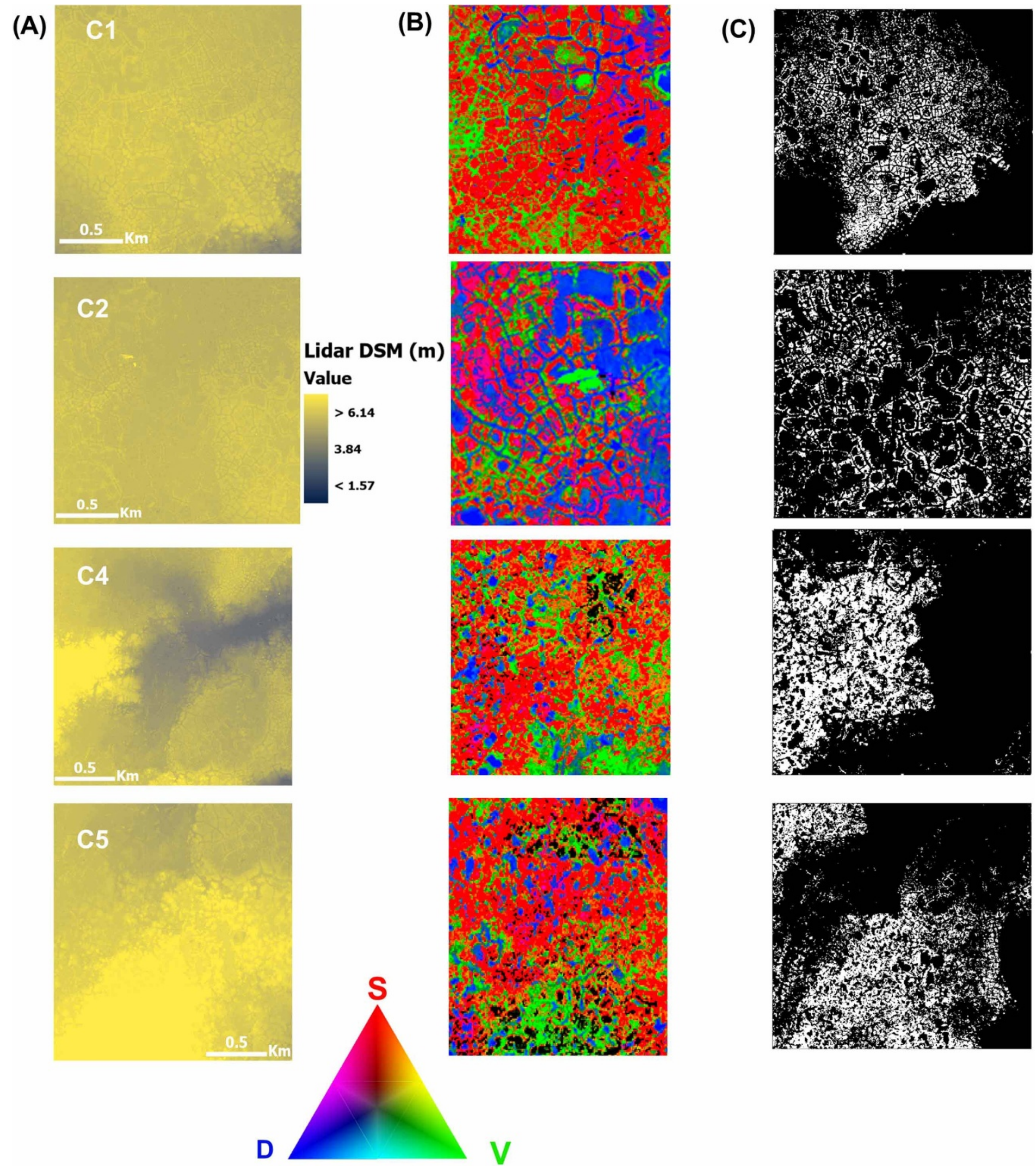

Figure 3. (A) Zoomed-in locations of clusters (C1, C2, C4, C5) of DSM, (B) SDV image, black pixels represent unvegetated thermokarst polygons and (C) threshold image applying the liberal threshold for soil the substrate band and liberal threshold for the lidar band, white pixels detecting probable unvegetated thermokarst polygons ($S = 50\%$, lidar $= 5$ m).

To quantify unvegetated thermokarst polygons detected by the unmixing analysis within the study area and to evaluate model performance of the field-based results, a joint probability analysis was conducted by fusing together the lidar band and the *S* band from the layer stacked unmixed image. The fusion of hyperspectral data and lidar has been previously used in classification studies to increase the accuracy of feature identification in remote sensing images (Qian *et al* 2023, Chen *et al* 2024), making it an appropriate approach for quantifying unvegetated thermokarst polygons. In the joint probability analysis, all possible combinations of the three thresholds presented earlier: conservative (90%), intermediate (70%), and liberal (50%) for the *S* band, and in addition conservative ($\geqslant$7.0 m), intermediate ($\geqslant$6.0 m), and liberal ($\geqslant$5.0 m) for the lidar band were explored. Water-related and infrastructure-related pixels were masked out in the joint probability analysis to improve the detection performance of unvegetated thermokarst polygons. This resulted in a total of nine decision rules, demonstrating all possible combinations of thresholds for the *S* and lidar band.

A threshold image was produced for each decision rule from the joint probability analysis to compile a confusion matrix that was used to evaluate the performance of the unmixing classification against the

Table 1. Confusion matrix analysis of predicted classification vs. Field verification.

Decision rule	Applied threshold	True positive	False positive	False negative	True negative	Precision	Recall	$F1$ score
Liberal soil with liberal lidar	Soil: 50% Lidar: ⩾5.0 m	24	10	18	0	0.71	0.57	0.63
Intermediate soil with liberal lidar	Soil: 70% Lidar: ⩾5.0 m	19	10	23	0	0.66	0.45	0.54
Conservative soil with liberal lidar	Soil: 90% Lidar: ⩾5.0 m	13	4	29	6	0.76	0.31	0.44
Liberal soil with conservative lidar	Soil: 50% Lidar: ⩾7.0 m	2	0	40	10	1	0.05	0.09

field-based results. Table 1 shows a summary of the models that had the best performance: liberal soil (50%) and liberal lidar (⩾5.0 m), intermediate soil (70%) and liberal lidar (⩾5.0 m); model that had average performance: conservative soil (90%) and liberal lidar (⩾5.0 m); and model that had poor performance: liberal soil (50%) and conservative lidar (⩾7.0 m). A complete set of all nine decision rules of the confusion matrix is shown in the supplementary material. A threshold image overlayed with coordinates from the 52 sites validated for the field-based results for each possible decision rule is included in the supplementary materials. The joint probability analysis and related threshold images were computed using ENVI® classic V.5.6.3. ENVI® is a registered trademark of NV5 Global, Inc. The final threshold images provided in the supplementary showing the location of the 52 sites from the field survey were generated using ArcGIS Pro 3.0.3 Copyright ©2022 Esri Inc. All rights reserved.

3. Results

Unvegetated polygons classified using the liberal soil and liberal lidar (LSLL) decision rule ($F1$ score 0.63 and recall 0.57, table 1) in the joint probability analysis most closely matched the field validation survey. From field classification, forty-two of the fifty-two sites hosting unvegetated thermokarst polygons were correctly classified (∼81% mapping success rate). Using these thresholds, the total predicted cover of unvegetated thermokarst polygons over the study area was 9.55% or 380 000 m^2 total area over the study site (table 2).

The confusion matrix (table 1, figure 4) of the field classification vs. predicted model classification for each decision rule in the joint probability analysis indicates that the models with combinations of LSLL, (ISLL—intermediate soil, liberal lidar) had the best model performance in terms of balanced precision and recall with $F1$ scores of approximately 0.63 and 0.54 respectively. The model such as (CSLL—conservative soil, liberal lidar), had moderate model performance with an $F1$ score of 0.44. On the weaker model performance end, the (LSCL—liberal soil, conservative lidar) had a low $F1$ score of 0.09. This indicates that a combination of the models with at least one liberal threshold was suitable for detecting unvegetated thermokarst polygons, and a sensitivity to lidar thresholds, for example, overly strict elevation thresholds resulted in lower precision model detection of unvegetated thermokarst polygons, and vice versa, with overly strict S band thresholds resulting in poor feature classification. A full table showing the complete set of values shown in figure 4 of the confusion matrix is provided in the supplementary.

From estimates of the liberal thresholds to determine individual band material frequency of S, V, and D from the spectrally unmixed image, we determined that one of the primary landscape properties relates to dark targets, likely associated with water (27.82%), followed by S-EM (26.53%). The frequency of pixels associated with V-EM is 18.5% (table 3, supplementary).

A classification of the vegetation types is shown in figure 5 based on the BAID high-resolution wetlands map (Tweedie *et al* 2016) shows graminoids and lichens dominated the vegetation near unvegetated thermokarst polygons. Patterns in vegetation near the unvegetated thermokarst polygons can be indicative of the environmental conditions of these features, such as the dominance of lichens on the edges of HCPs, which reflect drier soil moisture conditions. The spectral profiles of unvegetated thermokarst polygon features and nearby vegetation are shown in the supplementary material. These unvegetated thermokarst polygon features were generally at a higher elevation than the surrounding landscape, typically situated in areas with a maximum altitude of 8 m. Based on the NEON AOP lidar product, the mean elevation at which these features were detected was 6 m (with ranges from 4.1 m to

Table 2. Joint probability thresholds for estimating unvegetated thermokarst polygons EM abundances.

Study area extent = 4 km^2 or 4000 000 m^2			
Applied threshold	Percent of pixels in image (% of study area)	Mapped area (m^2)	Precision
Soil: 50% Lidar: ⩾5.0 m	9.55%	380 000	0.71
Soil: 70% Lidar: ⩾5.0 m	1.32%	50 000	0.66
Soil: 90% Lidar: ⩾5.0 m	0.06%	2000	0.76
Soil: 50% Lidar: ⩾7.0 m	0.09%	4000	1

the percentage or area covered in m^2 for the main decision rules from table 1 based on the joint-probability analysis.

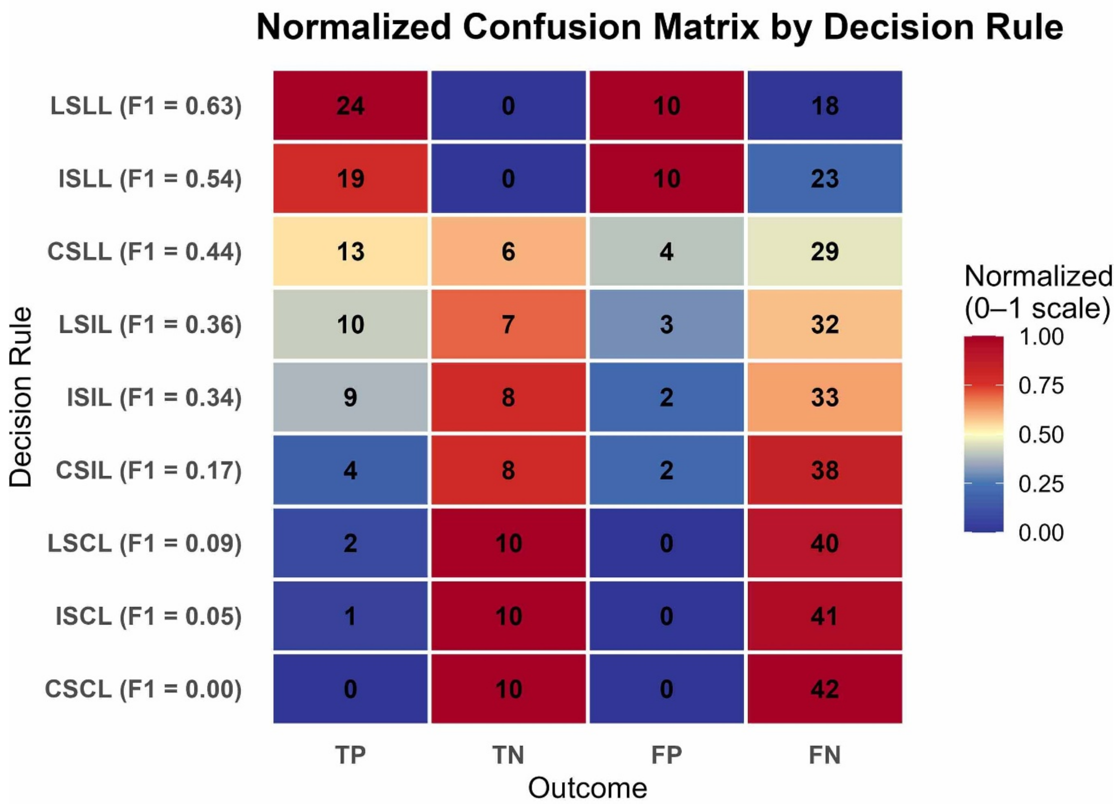

Figure 4. Heatmap of full confusion matrix (including all decision rules) of predicted classification vs. field verification. Decision rules are ranked from highest (top) to lowest *F*1 score (bottom). Key: CSCL—conservative soil and conservative lidar, CSIL—conservative soil and intermediate lidar, CSLL—conservative soil and liberal lidar, ISCL—intermediate soil and conservative lidar, ISIL—intermediate soil and intermediate lidar, ISLL—intermediate soil and liberal lidar, LSCL—liberal soil and conservative lidar, LSIL—liberal soil and intermediate lidar, LSLL—liberal soil and liberal lidar. For outcome: TP—true positive, TN—true negative, FP—false positive, FN—false negative.

6.8 m based on estimates calculated using the summarize elevation tool on ArcGIS Pro 3.0.3 Copyright ©2022 Esri Inc.). Approximately 97% of the unvegetated thermokarst polygons identified by this study were outside of the medium-age (50–300 yr) and old (300–2000 yr) drained lake basins (as classified by Hinkel *et al* 2003), indicating that unvegetated thermokarst polygons are likely to form in areas outside of drained thaw lakes and the timing of their formation in these areas can occur from anywhere between 50 and 2000 yrs after drainage.

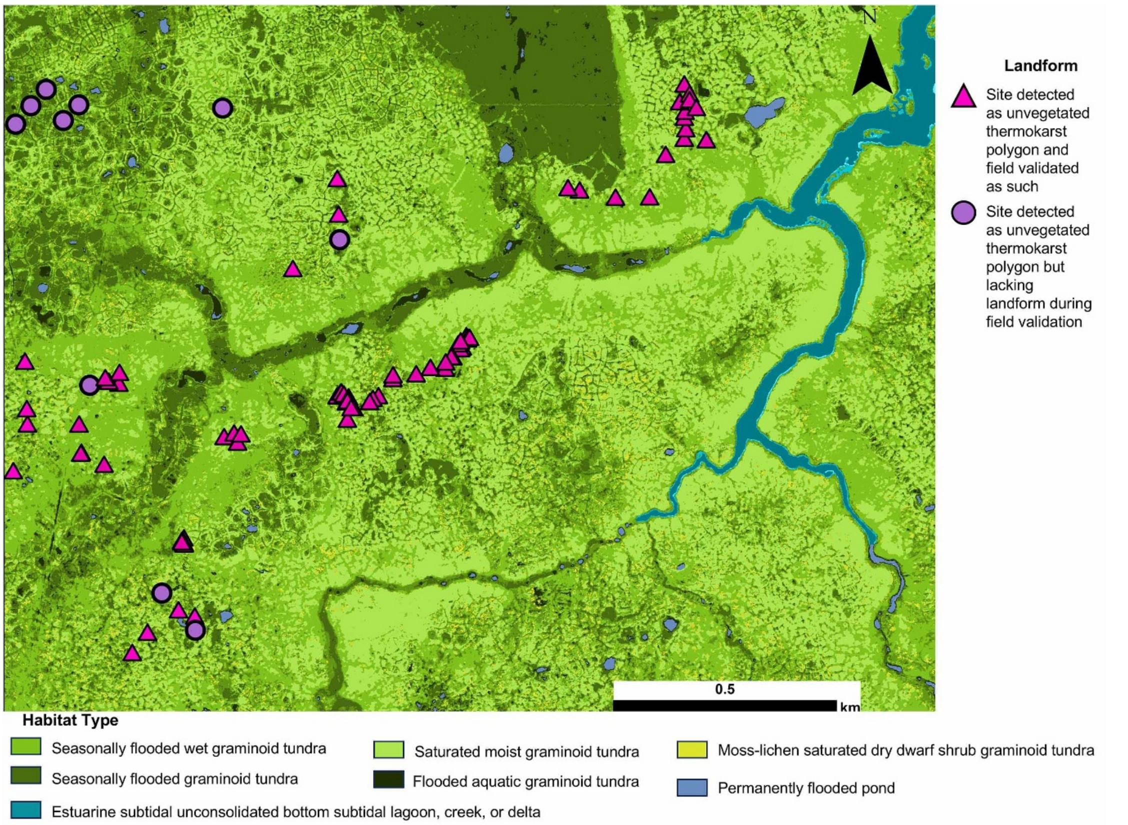

Figure 5. BAID wetlands map of the dominant vegetation types within the study extent (Tweedie *et al* 2016) overlaid with ground truth data collected throughout the field validation surveys (2022, 2023, 2025). Pink triangles (42 sites) show the location of features mapped as unvegetated thermokarst polygons by the unmixing analysis (figure 3) and validated as such in the field whereas purple circles (10 sites) show the location of features mapped as unvegetated thermokarst polygons, but landform was lacking during the field validation surveys. Reproduced with permission from Tweedie *et al* (2016). Map data ©2016 barrow area information database (BAID).

4. Discussion

The main objective in our study is to detect and provide estimates of unvegetated thermokarst polygons on Alaska's Arctic Coastal Plain using NEON AOP on the joint basis of imaging spectroscopy and lidar products at 1 m spatial resolution via SMA. These estimates consider microtographic landforms to contribute to estimates of thermokarst-affected land cover in Arctic regions. The LSLL threshold combination for soil and lidar from the confusion matrix evaluating threshold models of our analysis against field-based results had the greatest $F1$ score (0.63), along with balanced precision (0.71) and recall (0.57). Based on the results evaluating our remote sensing analyses against the field validation data, we estimate a 9.55% cover of unvegetated thermokarst polygons, or 380 000 m^2 total area of unvegetated thermokarst polygons within the study extent. Ground truth data from 52 sites revealed that the spectral mixture model correctly mapped ∼81% of unvegetated thermokarst polygons in the study area.

Incorporating microtopographic landforms (e.g. unvegetated thermokarst polygons) into the land-cover characterization of polygonized tundra and thermokarst-affected landscape on Alaska's Arctic Coastal Plain helps to refine land cover estimates, providing insight into permafrost destabilization and associated impacts on wildlife, infrastructure, and hydrological processes. Quantifying and detecting unvegetated thermokarst polygons can help identify the potential relevance of such land features and processes for the larger regional GHG budget from high-latitude ecosystems, particularly given the vast amount of carbon stored in thermokarst regions (Olefeldt *et al* 2016). Chamber flux studies on GHG emissions from thermokarst polygons in the BEO (Hashemi *et al* 2024) found that unvegetated thermokarst polygons were estimated to emit mean flux rates of 28 mg $N_2O{-}N$ ha^{-1} h^{-1}, adjusted for feature coverage of 1.5% of unvegetated thermokarst polygons based on UAV imagery over a limited area of their study region. Our estimates over a 4 km^2 area of the BEO places unvegetated thermokarst polygons at 9.5% coverage. Based on our estimates of unvegetated thermokarst polygons land cover, this brings mean N_2O emissions from these features to 178 mg N_2O–N ha^{-1} h^{-1} and CO_2 emissions to 36 g

CO_2 ha^{-1} h^{-1} at the landscape scale. Upscaling N_2O emissions based on adjusted estimates of feature coverage, based on our results, indicates that emissions are six times larger than previously estimated (Hashemi *et al* 2024) and closer to airborne eddy covariance estimates for the North Slope of Alaska at 3.8 (2.2–4.7) mg N_2O m^{-2} d^{-1} (Wilkerson *et al* 2019). Given the global warming potential of N_2O, which is 273 times that of CO_2 over a 100 yr time horizon (Forster *et al* 2021), our findings highlight the potential these features have to contribute to biogeochemical cycling. Regional coverage of unvegetated thermokarst polygons across thermokarst-affected landscapes remains uncertain, emphasizing the need for detection methods of these features in Arctic ecosystems.

The higher elevation of these unvegetated thermokarst polygon features is consistent with ground heave processes lifting the soil above the average elevation levels, likely connected to ice-wedge formation, melting, and polygon development (Liljedahl *et al* 2016). During the expansion of ice-wedges, the ground heaves, which influences the formation of HCPs (Liljedahl *et al* 2016), which is a key characteristic of the unvegetated thermokarst polygons mapped in our study. Interestingly, we found that these unvegetated thermokarst polygons were outside drained lake basins, likely because their formation occurs in higher elevation areas and follows the development of HCPs. The lack of vegetation in these features is probable in HCPs due to favorable conditions for frost heave action, and they are more exposed to wind abrasion, similar to peat palsas reported in Finland (Seppälä 2003).

Compared to *S*, *D*, and *V* EMs, unvegetated thermokarst polygons represented a lower frequency of pixel abundances of landscape material. The high pixel abundance of dark targets, likely linked to water, aligns with the wetland polygonal tundra characteristics of the study site located in a continuous permafrost zone. The higher frequency of pixels associated with dark targets likely confounded our selection of *S* materials within the unmixing analysis. This demonstrates the high spatial heterogeneity within the study site. In such areas, unvegetated thermokarst polygons may develop at different rates compared to Arctic areas in discontinuous permafrost zones, where warming and thermokarst development rates vary (Olefeldt *et al* 2021).

Previous work on detecting polygonal terrain, such as ice-wedges, using machine learning and deep learning techniques provides helpful insights into how these tools can be used with remote sensing techniques to enhance their capabilities. Zhang *et al* (2018) had an overall classification accuracy of 79% employing these methods to delineate ice wedge polygons in Northern Alaska. Witharana *et al* (2021) mapping of ice wedge polygons through using high spatial resolution commercial satellite imagery on sedge tundra had classification accuracies of correctness of 0.99, and on tussock tundra classification accuracies reporting correctness of 0.87. The study by Lousada *et al* (2018) using UAV and photogrammetric surveys found that mapping of ice wedge polygonal networks using remotely sensed images of very high resolution provides adequate support to classification and characterization of this type of terrain (Lousada *et al* 2018).

The ground-truth mapping success of ∼81% in our study highlights both the potential and the challenges of detecting unvegetated thermokarst polygons using imaging spectroscopy. A potential source of uncertainty in our analysis could be the misalignment in georeferencing between the remote sensing data and the field validation data. Even at the 1 m spatial resolution provided by the NEON AOP-derived datasets used in our analysis, the complexity of detecting the pure spectral signatures of physical properties of an ecosystem, such as soil in our case, is complex, as mixed pixels are likely to dominate in Arctic regions due to high heterogeneity even (Nelson *et al* 2022). As we observed in our study, SMA is a powerful tool for classifying materials, even in some of the most challenging ecosystems for applications of remote sensing techniques, such as polygonized tundra.

4.1. Limitations and future directions

An important aspect of our study is the use of remote sensing to understand surficial processes, particularly unvegetated thermokarst polygons. Limited studies within the Arctic Coastal Plain of Alaska have deployed optical remote sensing to study microtopography—primarily focusing on ice wedges and polygon development (Liljedahl *et al* 2016, Abolt and Young 2020). Our work presents a feasible approach for detecting and monitoring such landforms. By utilizing airborne imaging spectroscopy at a 1 m spatial resolution, we offer a detailed and effective method for observing these features. Our mapping efforts used data collected from one day of flights (11 July 2018) from the NEON AOP database. This imposes potential seasonal variability, in particular, vegetation phenology. Multi-temporal data collected throughout different periods (e.g. during the peak season and the fall period prior to snow) could refine polygon detection in future iterations and help develop the baselines for future investigation of the development of these features over temporal scales.

Future directions to detect unvegetated thermokarst polygons via optical remote sensing include a multi-platform approach with the available technology, such as leveraging drone-based measurements at finer spatial and spectral resolutions supplemented by hand-held spectroscopy to validate coarser products, such as satellite-borne. A combination of multi-scale measurements, as Nelson *et al* (2022) suggested for optimizing optical remote sensing in the Arctic, may be insightful to determine the extent of unvegetated thermokarst polygons, particularly in regions where airborne-derived imaging spectroscopy is lacking. Drone-based lidar could help improve sub-meter resolution and multispectral satellite imagery, such as Sentinel-2, for broader coverage of Arctic regions. The Polar Geospatial Center offers 50 cm DSM (ArcticDEM) data products throughout the Arctic that could be used in conjunction with multispectral Maxar's WorldView-2 satellite imagery at the meter scale for providing estimates in areas outside of NEON AOP flight domains. The fusion of SAR and topographic data to map polygonal terrain can be helpful, as demonstrated by Merchant *et al* (2024). Employing machine learning technologies such as convolutional neural networks, deep learning, and object-based classification also provides potential avenues for mapping microtographic features in Arctic landscapes such as ice wedge polygons (Zhang *et al* 2018, Witharana *et al* 2021, Merchant *et al* 2024). Additionally, laboratory measurements may supplement this, and novel platform techniques, such as tower-mounted observations (Nelson *et al* 2022), may provide key insights regarding the extent and processes associated with unvegetated thermokarst polygons.

It is important to identify the development of these features and their potential increase in coverage following increased temperatures and improve future predictions of thermokarst processes. This is critical to determine their role in the GHG budget from the Arctic. To leverage the characterization of landscapes via SMA, it may be helpful to use local and global EMs, including polar regions, to contribute to the accuracy of mapping efforts (Sousa *et al* 2022). Upscaling this approach provides a valuable opportunity to quantify unvegetated thermokarst polygon development across permafrost zones. Such efforts could also provide deeper insights into how different tundra types respond to global warming and its associated impacts on the carbon budget. This may help answer questions associated with spatiotemporal landscape patterns and provide insights into the overall status of an ecosystem and its functioning.

Acknowledgment

This study was funded by the Office of Polar Programs of the National Science Foundation (NSF) and awarded to D. Z., W. C. O. (Award Numbers 2149988 and 1932900) with additional support by the ABoVE (80NSSC21K1350) Program. The Alaskan sites are on land owned by the Ukpeaġvik Iñupiat Corporation (UIC). This study is supported and monitored by The National Oceanic and Atmospheric Administration—Cooperative Science Center for Earth System Sciences and Remote Sensing Technologies under the Cooperative Agreement Grant #: NA22SEC4810016. The authors would like to thank the NOAA Office of Education, The Educational Partnership Program with Minority Serving Institutions (NOAA-EPP/MSI) and the NOAA-CESSRST-II for full fellowship support for F.T. The statements, findings, conclusions and recommendations are those of the author(s) and do not necessarily reflect the views of NOAA. D.S. was supported by the USDA NIFA Sustainable Agroecosystems Program under Grant # 2022-67019-36397; the NASA Land-Cover/Land-Use Change Program under Grant # NNH21ZDA001N-LCLUC; the NASA Remote Sensing of Water Quality Program under Grant # 80NSSC22K0907; and the NSF Signals in the Soil Program under Award # 2226649. This material is based on services provided by the GAGE Facility, operated by EarthScope Consortium, with support from the National Science Foundation, the National Aeronautics and Space Administration, and the U.S. Geological Survey under NSF Cooperative Agreement EAR-1724794. The National Ecological Observatory Network is a program sponsored by the U.S. National Science Foundation and operated under cooperative agreement by Battelle. This material is based in part upon work supported by the U.S. National Science Foundation through the NEON Program.

We are grateful to the reviewers for their time in reviewing our manuscript and providing thoughtful suggestions that greatly improved the quality of our manuscript. F.T. is grateful to the Global Change Research Group for their help on and off the field and to Macall Hock, Marco Montemayor, Kim Peterson, and Claudia Peterson for their company throughout the field validation surveys.

Data availability statement

The data that support the findings of this study are openly available at the following URL/DOI: www.neonscience.org/data (NEON (National Ecological Observatory Network) 2025a, NEON (National Ecological Observatory Network) 2025b).

Supplementary Material for available at http://doi.org/10.1088/2752-664X/ae487e/data1.

CSCL available at http://doi.org/10.1088/2752-664X/ae487e/data2.

ISCL available at http://doi.org/10.1088/2752-664X/ae487e/data3.
LSCL available at http://doi.org/10.1088/2752-664X/ae487e/data4.
CSIL available at http://doi.org/10.1088/2752-664X/ae487e/data5.
ISIL available at http://doi.org/10.1088/2752-664X/ae487e/data6.
LSIL available at http://doi.org/10.1088/2752-664X/ae487e/data7.
CSLL available at http://doi.org/10.1088/2752-664X/ae487e/data8.
ISLL available at http://doi.org/10.1088/2752-664X/ae487e/data9.
LSLL available at http://doi.org/10.1088/2752-664X/ae487e/data10.
Fig. S1 available at http://doi.org/10.1088/2752-664X/ae487e/data11.
neonapo_beo_endmembers.csv available at http://doi.org/10.1088/2752-664X/ae487e/data12.

Conflict of interest

The authors declare no competing interests.

ORCID iDs

F Tenorio 0009-0000-3398-1085
D Sousa 0000-0002-1632-1955
J Hashemi 0000-0002-8660-7406
S J Davidson 0000-0001-8327-2121
W C Oechel 0000-0002-3504-026X
C E Tweedie 0000-0002-3409-8881
B D Thomas 0000-0001-8763-6148
S Rauschenbach 0000-0003-0747-3022
D Zona 0000-0002-0003-4839

References

Abbott B W and Jones J B 2015 Permafrost collapse alters soil carbon stocks, respiration, CH_4, and N_2O in upland tundra *Glob. Change Biol.* **21** 4570–87
Abolt C J and Young M H 2020 High-resolution mapping of spatial heterogeneity in ice wedge polygon geomorphology near Prudhoe Bay, Alaska *Sci. Data* **7** 87
Adams J B and Gillespie A R 2006 Spectral-mixture analysis *Remote Sensing of Landscapes with Spectral Images: A Physical Modeling Approach* (Cambridge University Press) pp 126–67
Adams J B, Smith M O and Johnson P E 1986 Spectral mixture modeling: a new analysis of rock and soil types at the Viking Lander 1 Site *J. Geophys. Res.* **91** 8098
Arndt K A, Santos M J, Ustin S, Davidson S J, Stow D, Oechel W C and Zona D 2019 Arctic greening associated with lengthening growing seasons in Northern Alaska *Environ. Res. Lett.* **14** 125018
Billings W D and Peterson K M 1980 Vegetational change and ice-wedge polygons through the thaw-lake cycle in Arctic Alaska *Arct. Alp. Res.* **12** 413–32
Black R F 1964 *Gubik Formation of Quaternary Age in Northern Alaska* (US Government Printing Office)
Boardman J W 1995 Analysis, understanding, and visualization of hyperspectral data as convex sets in n space *Proc. SPIE* **2480** 14–22
Bockheim J G, Everett L R, Hinkel K M, Nelson F E and Brown J 1999 Soil organic carbon storage and distribution in Arctic Tundra, Barrow, Alaska *Soil Sci. Soc. Am. J.* **63** 934–40
Bockheim J G and Tarnocai C 1998 Recognition of cryoturbation for classifying permafrost-affected soils *Geoderma* **81** 281–93
Britton M E 1957 Vegetation of the arctic tundra
Brown J, Everett K R, Webber P J, MacLean S F Jr and Murray D F 1980 The coastal tundra at Barrow *An Arctic Ecosystem: The Coastal Tundra at Barrow, Alaska* vol 12 (Dowden, Hutchinson & Ross, Inc.) pp 1–29
Bryan K 1946 Cryopedology—the study of frozen ground and intensive frost action with suggestions on nomenclature *Am. J. Sci.* **244** 622–42
Chen T, Chen S, Chen L, Chen H, Zheng B and Deng W 2024 Joint classification of hyperspectral and LiDAR data via multiprobability decision fusion method *Remote Sens.* **16** 4317
Chowdhury T, Herndon E M, Phelps T J, Elias D A, Gu B, Liang L, Wullschleger S D and Graham D E 2015 Stoichiometry and temperature sensitivity of methanogenesis and CO_2 production from saturated polygonal tundra in Barrow, Alaska *Glob. Change Biol.* **21** 722–37
Davidson S, Santos M, Sloan V, Watts J, Phoenix G, Oechel W and Zona D 2016a Mapping Arctic tundra vegetation communities using field spectroscopy and multispectral satellite data in North Alaska, USA *Remote Sens.* **8** 978
Fiencke C, Marushchak M E, Sanders T, Wegner R and Beer C 2022 Microbiogeochemical traits to identify nitrogen hotspots in permafrost regions *Nitrogen* **3** 458–501
Forster P, Storelvmo T, Armour K, Collins W, Dufresne J-L, Frame D, Lunt D, Mauritsen T, Palmer M and Watanabe M 2021 The Earth's energy budget, climate feedbacks, and climate sensitivity
Gillespie A 1990 Interpretation of residual images: spectral mixture analysis of AVIRIS images, Owens Valley, California *Proc. second airborne visible/infrared imaging spectrometer (AVIRIS) Workshop*
Harden J W *et al* 2012 Field information links permafrost carbon to physical vulnerabilities of thawing *Geophys. Res. Lett.* **39** 15
Hashemi J, Lipson D A, Arndt K A, Davidson S J, Kalhori A, Lunneberg K, van Delden L, Oechel W C and Zona D 2024 Thermokarst landscape exhibits large nitrous oxide emissions in Alaska's coastal polygonal tundra *Commun. Earth Environ.* **5** 473

Hinkel K M, Eisner W R, Bockheim J G, Nelson F E, Peterson K M and Dai X 2003 Spatial extent, age, and carbon stocks in drained thaw lake basins on the Barrow Peninsula, Alaska *Arctic Antarctic Alpine Res.* **35** 291–300

Hugelius G *et al* 2014 Estimated stocks of circumpolar permafrost carbon with quantified uncertainty ranges and identified data gaps *Biogeosciences* **11** 6573–93

Jones B M, Grosse G, Arp C D, Jones M C, Walter Anthony K M and Romanovsky V E 2011 Modern thermokarst lake dynamics in the continuous permafrost zone, northern Seward Peninsula, Alaska *J. Geophys. Res.* **116** G2

Jorgenson M T, Shur Y L and Pullman E R 2006 Abrupt increase in permafrost degradation in Arctic Alaska *Geophys. Res. Lett.* **33** 2

Kanevskiy M *et al* 2022 The shifting mosaic of ice-wedge degradation and stabilization in response to infrastructure and climate change, Prudhoe Bay Oilfield, Alaska, USA *Arct. Sci.* **8** 498–530

Kanevskiy M, Shur Y, Jorgenson T, Brown D R, Moskalenko N, Brown J and Buchhorn M 2017 Degradation and stabilization of ice wedges: implications for assessing risk of thermokarst in northern Alaska *Geomorphology* **297** 20–42

Kaplan J O *et al* 2003 Climate change and Arctic ecosystems: 2. Modeling, paleo data-model comparisons, and future projections *J. Geophys. Res.* **108** D19

Kokelj S V and Jorgenson M T 2013 Advances in thermokarst research *Permafrost Periglacial Process.* **24** 108–19

Lachenbruch A H 1962 *Mechanics of Thermal Contraction Cracks and Ice-wedge Polygons in Permafrost* vol 70 (Geological Society of America)

Lara M J, Chen Y and Jones B M 2021 Recent warming reverses forty-year decline in catastrophic lake drainage and hastens gradual lake drainage across northern Alaska *Environ. Res. Lett.* **16** 124019

Lara M J, Chipman M L and Hu F S 2019 Automated detection of thermoerosion in permafrost ecosystems using temporally dense Landsat image stacks *Remote Sens. Environ.* **221** 462–73

Lara M J, McGuire A D, Euskirchen E S, Tweedie C E, Hinkel K M, Skurikhin A N, Romanovsky V E, Grosse G, Bolton W R and Genet H 2015 Polygonal tundra geomorphological change in response to warming alters future CO2 and CH4 flux on the Barrow Peninsula *Glob. Change Biol.* **21** 1634–51

Leffingwell E D K 1915 Ground-ice wedges: the dominant form of ground-ice on the North Coast of Alaska *J. Geol.* **23** 635–54

Liljedahl A K *et al* 2016 Pan-Arctic ice-wedge degradation in warming permafrost and its influence on tundra hydrology *Nat. Geosci.* **9** 312–8

Lin D H, Johnson D R, Andresen C and Tweedie C E 2012 High spatial resolution decade-time scale land cover change at multiple locations in the Beringian Arctic (1948–2000s) *Environ. Res. Lett.* **7** 025502

Liu L, Schaefer K, Gusmeroli A, Grosse G, Jones B M, Zhang T, Parsekian A D and Zebker H A 2014 Seasonal thaw settlement at drained thermokarst lake basins, Arctic Alaska *The Cryosphere* **8** 815–26

Lousada M, Pina P, Vieira G, Bandeira L and Mora C 2018 Evaluation of the use of very high resolution aerial imagery for accurate ice-wedge polygon mapping (Adventdalen, Svalbard) *Sci. Total Environ.* **615** 1574–83

Marushchak M E, Pitkämäki A, Koponen H, Biasi C, Seppälä M and Martikainen P J 2011 Hot spots for nitrous oxide emissions found in different types of permafrost peatlands *Glob. Change Biol.* **17** 2601–14

Merchant M, Bourgeau-Chavez L, Mahdianpari M, Brisco B, Obadia M, DeVries B and Berg A 2024 Arctic ice-wedge landscape mapping by CNN using a fusion of Radarsat constellation Mission and ArcticDEM *Remote Sens. Environ.* **304** 114052

Muller S W 1943, 1945, 1947 *Permafrost or Permanently Frozen Ground and Related Engineering Problems* (Strategic Engineering Study 62, US. Army Engineers. Second printing with corrections, 1945. Litho-printed, Ann Arbor, A4kh, 1947) pp 231pp

National Research Council 2014 *Opportunities to use remote sensing in understanding permafrost and related ecological characteristics: Report of a workshop* (National Academies Press)

Nelson P R *et al* 2022 Remote sensing of tundra ecosystems using high spectral resolution reflectance: opportunities and challenges *J. Geophys. Res.* **127** e2021JG006697

NEON (National Ecological Observatory Network) 2025a Elevation—LiDAR (DP3.30024.001), RELEASE-2025 (available at: https://data.neonscience.org/data-products/DP3.30024.001/RELEASE-2025) (Accessed 4 February 2025)

NEON (National Ecological Observatory Network) 2025b Spectrometer orthorectified surface directional reflectance—mosaic (DP3.30006.001), RELEASE-2025 (available at: https://data.neonscience.org/data-products/DP3.30006.001/RELEASE-2025)) (Accessed 4 February 2025)

NOAA National Centers for Environmental Information 2023 Monthly global climate report for annual 2022 (available at: www.ncei.noaa.gov/access/monitoring/monthly-report/global/202213.www.ncei.noaa.gov/access/metadata/landing-page/bin/iso?id=gov.noaa.ncdc:C00672) (Accessed 3 February 2025)

Oechel W C, Hastings S J, Vourlitis G, Jenkins M, Riechers G and Grulke N 1993 Recent change of Arctic tundra ecosystems from a net carbon dioxide sink to a source *Nature* **361** 520–3

Olefeldt D *et al* 2016 Circumpolar distribution and carbon storage of thermokarst landscapes *Nat. Commun.* **7** 13043

Olefeldt D, Heffernan L, Jones M C, Sannel A B K, Treat C C and Turetsky M R 2021 Permafrost thaw in northern peatlands: rapid changes in ecosystem and landscape functions *Ecosystem Collapse and Climate Change* (Springer) pp 27–67

Peterson R A and Krantz W B 2008 Differential frost heave model for patterned ground formation: corroboration with observations along a North American arctic transect *J. Geophys. Res.* **113** G3

Péwé T L 1954 Effect of permafrost on cultivated fields, Fairbanks Area, Alaska. U.S *Geol. Surv. Bull.* **989-F** 315–51

Péwé T L 1969 *The periglacial environment* (McGill-Queen's University Press) pp 1–9

Qian D, Wei L and Chiru G 2023 Hyperspectral and LiDAR Data Fusion *Advances in Hyperspectral Image Processing Techniques* (IEEE) pp 279–92

Rantanen M, Karpechko A Y, Lipponen A, Nordling K, Hyvärinen O, Ruosteenoja K and Laaksonen A 2022 The Arctic has warmed nearly four times faster than the globe since 1979 *Commun. Earth Environ.* **3** 168

Raynolds M K, Walker D A, Ambrosius K J, Brown J, Everett K R, Kanevskiy M, Kofinas G P, Romanovsky V E, Shur Y and Webber P J 2014 Cumulative geoecological effects of 62 years of infrastructure and climate change in ice-rich permafrost landscapes, Prudhoe Bay Oilfield, Alaska *Glob. Change Biol.* **20** 1211–24

Raynolds M K, Walker D A and Maier H A 2005 Plant community-level mapping of arctic Alaska based on the circumpolar arctic vegetation map *Phytocoenologia* **35** 821

Repo M E, Susiluoto S, Lind S E, Jokinen S, Elsakov V, Biasi C, Virtanen T and Martikainen P J 2009 Large N_2O emissions from cryoturbated peat soil in tundra *Nat. Geosci.* **2** 189–92

Seppälä M 2003 Surface abrasion of palsas by wind action in Finnish Lapland *Geomorphology* **52** 141–8

Settle J and Drake N 1993 Linear mixing and the estimation of ground cover proportions *Int. J. Remote Sens.* **14** 1159–77

Shur Y, Jones B M, Jorgenson M T, Kanevskiy M Z, Liljedahl A, Walker D A, Ward Jones M K, Fortier D and Vasiliev A 2025 Formation of low-centered ice-wedge polygons and their orthogonal systems: a review *Geosciences* **15** 249

Smith M O, Ustin S L, Adams J B and Gillespie A R 1990 Vegetation in deserts: I. A regional measure of abundance from multispectral images *Remote Sens. Environ.* **31** 1–26

Sousa D, Brodrick P, Cawse-Nicholson K, Fisher J B, Pavlick R, Small C and Thompson D R 2022 The spectral mixture residual: a source of low-variance information to enhance the explainability and accuracy of surface biology and geology retrievals *J. Geophys. Res.* **127** e2021JG006672

Sousa D and Small C 2019 Globally standardized MODIS spectral mixture models *Remote Sens. Lett.* **10** 1018–27

Sousa D and Small C 2023 Topological generality and spectral dimensionality in the Earth Mineral Dust Source Investigation (EMIT) using joint characterization and the spectral mixture residual *Remote Sens.* **15** 2295

Stow D A *et al* 2004 Remote sensing of vegetation and land-cover change in Arctic Tundra Ecosystems *Remote Sens. Environ.* **89** 281–308

Tweedie C E, Villarreal S, Andresen C and Cody R. 2016, Detailed wetlands map for the Barrow Region, northern Alaska, for 2010–2013: barrow area information database (BAID), digital media (available at: http://barrowmapped.org).

Van Everdingen R O International Permafrost Association 1998 *Multi-language Glossary of Permafrost and Related Ground-ice Terms in Chinese, English, French, German* (Arctic Inst. of North America University of Calgary)

Villarreal S, Hollister R D, Johnson D R, Lara M J, Webber P J and Tweedie C E 2012 Tundra vegetation change near Barrow, Alaska (1972–2010) *Environ. Res. Lett.* **7** 015508

Voigt C, Marushchak M E, Abbott B W, Biasi C, Elberling B, Siciliano S D, Sonnentag O, Stewart K J, Yang Y and Martikainen P J 2020 Nitrous oxide emissions from permafrost-affected soils *Nat. Rev. Earth Environ.* **1** 420–34

Wainwright H M, Dafflon B, Smith L J, Hahn M S, Curtis J B, Wu Y, Ulrich C, Peterson J E, Torn M S and Hubbard S S 2015 Identifying multiscale zonation and assessing the relative importance of polygon geomorphology on carbon fluxes in an Arctic tundra ecosystem *J. Geophys. Res.* **120** 788–808

Wilkerson J, Dobosy R, Sayres D S, Healy C, Dumas E, Baker B and Anderson J G 2019 Permafrost nitrous oxide emissions observed on a landscape scale using the airborne eddy-covariance method *Atmos. Chem. Phys.* **19** 4257–68

Witharana C *et al* 2021 An object-based approach for mapping tundra ice-wedge polygon troughs from very high spatial resolution optical satellite imagery *Remote Sens.* **13** 558

Yang G *et al* 2018 Magnitude and pathways of increased nitrous oxide emissions from uplands following permafrost thaw *Environ. Sci. Technol.* **52** 9162–9

Zhang W, Witharana C, Liljedahl A K and Kanevskiy M 2018 Deep convolutional neural networks for automated characterization of arctic ice-wedge polygons in very high spatial resolution aerial imagery *Remote Sens.* **10** 1487

Zona D *et al* 2009 Methane fluxes during the initiation of a large-scale water table manipulation experiment in the Alaskan Arctic tundra *Glob. Biogeochem. Cycles* **23** n/a